Univerzita Komenského v Bratislave
Fakulta matematiky, fyziky a informatiky

Marco Enrico Biagio Pelletta

Autoreferát dizertačnej práce

In-situ study of copper growth on 2D materials

na získanie akademického titulu philosophiae doctor

v odbore doktorandského štúdia:
4.1.4. kvantová elektronika a optika

Miesto a dátum: Bratislava **03.05.2018**

Dizertačná práca bola vypracovaná v dennej forme doktorandského štúdia na Fyzikálnom ústave Slovenskej akadémie vied

Predkladatel': Marco Enrico Biagio Pelletta
Fyzikálny ústav, SAV
Dúbravská cesta 9
845 11 Bratislava

Školitel': Dr. Rer. Nat Peter Šiffalovič, PhD.
Fyzikálny ústav, SAV

4.1.4. kvantová elektronika a optika
(študijný odbor) (názov študijného programu doktorandského štúdia)

Predseda odborovej komisie:
.....
(meno a priezvisko s uvedením titulov a hodností
a presná adresa jeho zamestnávatel'a)

ABSTRACT

Graphene and MoS_2 monolayers are materials with promising applications in the electronics and semiconductors industries and the study of how the metals are growing on them is a topic of great interest for both cost-effective surface-supported catalysis applications and contacts improvement, that translates into better devices performances. In particular, copper is a standard material for fabrication of conductive contacts and it exhibits a Volmer-Weber growth dynamics on both graphene and MoS_2. This mode is characterized by the formation of 3D islands and considerable differences in the growth kinetics may arise from different copper adatom adsorption and diffusion energies. The real space in-situ studies often include sophisticated experimental setups having metal evaporators combined with transmission electron microscope or scanning probe microscopes. The real space techniques are particularly efficient in the characterization of the early stages of thin film growth, especially in the nucleation stage, but their employment in-situ is complex and not always feasible, while performing these techniques ex-situ implies the end of the deposition process. Instead, the measurements in reciprocal space rely on the scattering of X-ray photons or electrons, they are non destructive and can be performed in-situ during the deposition process. For this reason, herein it is presented a unique laboratory-based grazing-incidence small-angle X-ray scattering (GISAXS) technique which allows to track the temporal evolution of the copper thin film growth on graphene and MoS_2 surfaces. The influence of the substrate temperature is studied for both the set of experiments performed on graphene and on MoS_2. The geometry of the graphene samples allowed a comparison of the GISAXS results with the in-situ ellipsometric measurements. In all the GISAXS datasets collected at various temperatures, it is possible to recognize three main growth stages, namely nucleation and cluster growth, dynamic coalescence and early stage of percolation. An analysis of the nucleation density and how the temperature affects it, enhancing the mobility of the copper adatoms,

is presented for both the sets of experiments. The experimental results achieved show the importance of in-situ GISAXS studies for a real-time growth monitoring of copper and other noble metals on 2D materials and this work demonstrates the potential of laboratory-based in situ GISAXS as a vital diagnostic tool for tailoring a large variety of Cu nanostructures on graphene and MoS_2 monolayer based materials.

Contents

1. Introduction **3**

2. Theory **4**

3. Experimental setup: design and development **7**

4. Results and conclusions **9**
   - **4.1 Thermal evaporation deposition on graphene** 9
   - **4.2 Thermal evaporation deposition on molybdenum disulphide** 14

5. List of publications **18**
   - **5.1 Publications in CC journals** 18
   - **5.2 Publications in book's chapters** 19
   - **5.3 Conference's contributions** 19

1. INTRODUCTION

The discovery of graphene in 2004 [1] constituted a turning point for the modern experimental physics. This material granted the Nobel prizes to Novoselov and Geim for its discovery and thanks to its multiple properties it became object of study leading to the creation of a global market around it for the value of $12 million by 2013 [2]. Moreover, this discovery led to address novel attention to the properties, attributes and employment possibility of other 2D materials as the MoS_2 and to the surface science in general. The modern electronics widely employs semiconductor devices in order to create logic doors as well as sensors or amplifiers in the circuitry. For their optimal performances a fine control over the charge carriers and their flow is needed. This can be partially achieved thanks to a good quality of the electrical contacts, in fact, the lower their resistivity is, the better they are able to transfer the carriers injected in them to the semiconducting material. Creating contacts on 2D semiconductors is a task that poses different challenges, conceptual as well as practical, but, achieving low contact resistance in devices based on 2D semiconductor is necessary in order to have large photoresponse [3], high 'on' current and high-frequency operations [4]. In order to achieve these results, as pointed out by other authors [5, 6], the investigations on metals nucleation even at the single monomer level can provide important insights for metals/2D materials contacts and still remain an open field of study. There exists a quantum limit for the contact resistance (R_C^{min}) which is given by the number of conducting modes that the semiconductor channel can sustain [7, 8] and is connected to the 2D charge carrier density (n_{2D}) but, nowadays, we are still far from this limit.

2. THEORY

The growth of thin films occurs in three processes:

- Firstly the material to be deposited is separated from the source through the heating of the target, as in our case, or for high voltage extraction.
- Then the extracted particles ejected form the target travel toward the prefixed substrate.
- Eventually the particles reach the substrate surface where they are adsorbed.

  This last process can be further decomposed in various steps:

  - Thermal accommodation is the first passage that the imping particles must fulfil in order to be adsorbed on the sample surface, in particular, they must thermally lose enough of their kinetics energy in order to adhere to the surface.
  - After the particles are accommodated on the substrate the binding follows. This may happens through physisorption, when the particles form weak Van der Waals bonds, typically of the order of 0.01 eV., with the atoms of the bulk, as in our case, or through chemisorption, when the particles form strong chemical bonds, typically of a magnitude comprised between 1 and 10 eV., with the atoms of the bulk.
  - Once that the particles incoming on the sample have formed the bonds with the most external atoms of the bulk, there occurs the phenomenon of surface diffusion.
  - Nucleation is the method through which the clusters form and is characterized by two competitive processes, when the clusters have a condensation energy per unit volume ΔG_V which lowers the desorption rate their growth is encouraged, while, when they have a surface energy

higher than the one of individual atoms the breaking up of the clusters is encouraged, in order to minimize energy.

- Subsequently to a successful nucleation the formed islands experience a growth. Experimentally have been observed three different modes of islands growth:
  - In the case of a Volmer - Weber kinetics the clusters grow separately on the substrate forming three dimensional islands. This situation typically occurs when the atoms are more strongly bound to each others than to the substrate and/or in conditions of slow diffusion on the substrate surface [9], as in our case.
  - In the case of a Frank - van der Merwe kinetics the clusters merge together in wide planar structures determining a layer by layer growth. This situation typically occurs when the atoms are more strongly bound to the substrate than to each other and/or in conditions of fast diffusion.
  - In the case of a Stranski - Krastanov kinetics some of the clusters merge together while others grow separately determining a mixed growth in which islands are emerging from a coalesced layer. This growth process is typically divided into two phases, initially due to the fact that the atoms are more strongly bound to the substrate than to each other and/or there occurs a fast diffusion phenomenon, a layer by layer growth is encouraged, then, after one or more layers are formed, a change in the energetics, that determines a decrease of the diffusion on the structure, verifies and the imping particles tend now to set when they reach the deposited layer not changing their landing positions, therefore, three dimensional islands start to emerge [9].

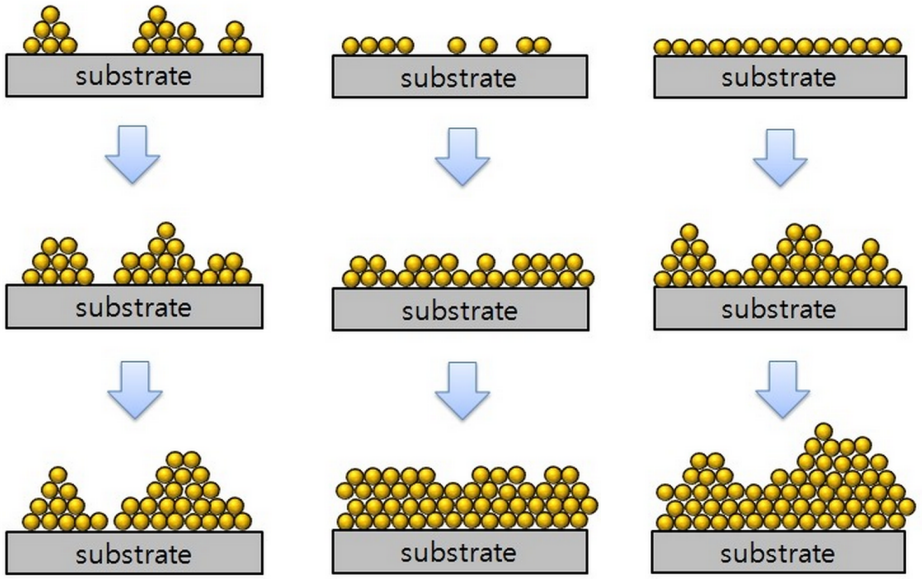

(a) Volmer - Weber growth model. *(b)* Frank - van der Merwe growth model. *(c)* Stranski - Krastanov growth model.

Fig. 2.1: Schematic of the three different types of growth that can follow a thin film [10]

- Once sufficiently big islands are formed, they undergo to the coalescence process, where smaller clusters merge together in bigger islands.
- Finally the structures formed till this point can experience percolation and continued growth depending on parameters as the bulk or the surface diffusion, the desorption, the geometry of the merged structures, in fact, the presence of shadowing effects limits the possibility of a further homogeneous growth of the deposited layer because the successive impinging particles will find, already formed, irregular islands on their trajectories [9].

3. EXPERIMENTAL SETUP: DESIGN AND DEVELOPMENT

The growths are performed inside a deposition chamber customly designed that has a vacuum pressure in working conditions of $2 * 10^{-8}$ mbar and a partial oxygen pressure of $4 * 10^{-9}$ mbar. The pressure is kept constant thanks to the combination of a scroll pump and a turbopump. This deposition chamber presents two beryllium windows for X-Rays to allow in-situ GISAXS measurements, one at the bottom where the X-Rays are going to enter in the chamber and the other at the top, before the detector. Furthermore, other two transparent windows are present, one in the lower emisphere of the chamber and the other in the upper one, in order to allow ellypsometric in-situ measurements. These configurations are depicted in the schematic of fig. 3.1.

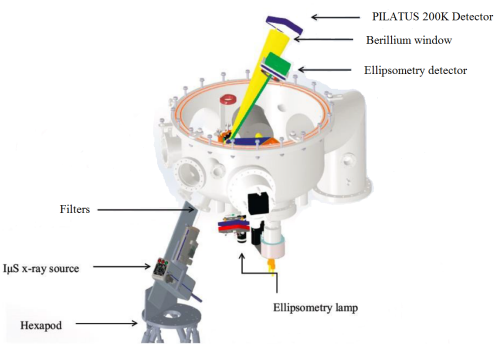

Fig. 3.1: Schematic drawing of the GISAXS and ellipsometry set-ups in the deposition chamber.

The X-Ray beam employed to perform the GISAXS measurements has a wave-length of 0.154 nm and is generated by a 30 W microfocus X-Ray source equipped with a focusing Montel optics that produces a beam with a divergence of 1 mrad. A pinhole of 1 mm diameter realized from a Ge crystal is fixed inside the chamber, before the stage where the sample is placed, in order to remove the parasitic X-Ray scattering from the multilayer Montel optics and define the beam size. An X-Ray detector made of 2D complementary metal oxide semiconductor (CMOS)-based hybrid is used to integrate the radiation scattered by the sample and the integration time defined for the acquisition of every frame is set to 5 seconds, during which the intensity is integrated in a continuous loop without interrupting the

Cu deposition process. The intensity collected from each pixel $I(\vec{q}) \approx |F(\vec{q})|^2 S(\vec{q})$ is the result of the product between the interference function, given by the Fourier transform of the pair correlation function of the nanostructures position $S(\vec{q}) \approx \int C(\vec{r}) e^{i\vec{q}\vec{r}} dr$ and the square modulus of the mean nanostructure form factor, given by the Fourier transform of electron density $F(\vec{q}) \approx \int\int\int \rho(\vec{r}) e^{-i\vec{q}vecr} dV$. The sample is positioned on a holder in the center of the chamber in a geometry that allows both the deposition process and the characterization by GISAXS and ellypsometry. The deposition chamber is connected to a load-lock chamber that permits the introduction of a new sample and the extraction of a deposited one without compromising the vacuum and the environment inside the main chamber. To perform the deposition through thermal evaporation we inserted a crucible in the chamber and an ultra pure copper ball obtained from the cutting and the folding of a copper foil was positioned in the basket of the crucible. The crucible extremities were connected to the two internal wires of a flange connector. Its two external conductive pins were successively plugged to a power supply. A pneumatic shutter is placed between the evaporator and the sample holder and can be used to inhibit the deposition in order to define the duration of the deposition process and the thickness of the deposited film. Some testing on silicon and then on graphene samples helped to find the best experimental parameters. The depositions were performed on samples heated and kept at constant different temperatures. After an initial annealing at 250°C for two hours common to all the samples, each one was heated at a constant predefined temperature for all the duration of the deposition process. In-situ GISAXS and ellipsometric measurement were acquired for the experiments performed on the graphene substrate, while, for geometry constraints, only GISAXS measurements were acquired for the experiments performed on MoS_2. The final films thicknesses after the Cu depositions were measured ex-situ using a stylus profilometer in order to retrieve the deposition rate for which we found an almost constant value of 0.25 Å/s for all the experiments. Further depositions were performed at the constant temperatures of 50°C and 200°C for graphene and at 60°C, 100°C and 150°C for MoS_2 in order to permit an ex-situ analysis by real-space techniques, namely the AFM, and for all the samples a Cu layer with an equivalent thickness of 4 nm was grown.

4. RESULTS AND CONCLUSIONS

4.1 Thermal evaporation deposition on graphene

The purpose of this sets of experiments was to characterize the growth of the Cu deposited by thermal evaporation and the kinetics dependence on the substrate temperature. I developed a model based on the Drude one, to describe the behaviour of the mobile electrons in the outern shells, and on three Lorentz oscillators, two focused on the optical transition of the copper 3d band and a smaller one to describe higher energy transitions, in accordance with the density of states diagram of copper [11], in order to fit the ellipsometric data. The growing of clusters during the deposition strongly depends on the surface free energy and on the binding energy of the incoming material. If we limit our attention to the surfaces free energies and consider the adsorbed material as a liquid drop on a solid substrate it is possible to define a spreading parameter S [12], able to describe the wetting phenomenon, with the formula:

$$S = \gamma_s - \gamma_l - \gamma_{s-l} \tag{4.1}$$

Where γ_s is the surface energy of the substrate, γ_l is the one of the liquid and γ_{s-l} is the interfacial energy between the substrate and the liquid. When $S > 0$ the liquid completely wets the substrate, while when $S < 0$ the liquid partially wets the substrate. Considering now the case of the graphene substrate, the value of the surface energy for graphene is 100 $\frac{mJ}{m^2}$, while for copper this value rises to 1830 $\frac{mJ}{m^2}$, that is more than one order of magnitude higher respect to the first one [13]. From these values it is immediate to relize that the spreading parameter is negative, leading to a partial wetting of the copper on the graphene surface and determining a growing mechanism of type Volmer-Weber, with the formation of big islands instead of a continuous layer. The same occurs for the MoS_2 and both behaviours were confirmed by the AFM measurements. Considering the GISAXS patterns

recorded for the depositions on graphene for each frame belonging to a constant deposition temperature it is possible to extract the intensity profile of a cut along the q_y direction at the critical exit angle. The interference function starts to arise and become well defined in the X-Ray scattering profiles for a copper deposited thickness of around 1 nm, anyway, it results hard to find the maximum of the initial streak with precision, leading to data with high uncertainty, until a better defined peak appears. In order to retrieve quantitative peak parameters, the extracted profiles were fitted with the combination of a Gaussian and an exponential decaying function. The position of the maximum of the Gaussian in the reciprocal space $q_{y,max}$ is shown in fig. 4.1 as a function of the deposited copper thickness.

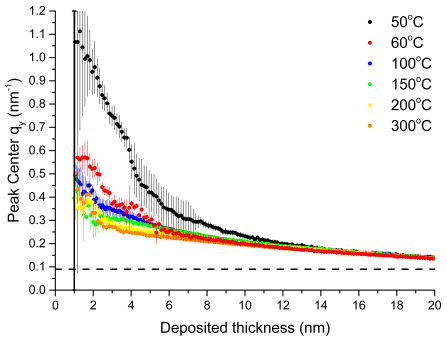

Fig. 4.1: Plot of the $q_{y,max}$ vs. deposited copper thickness for various deposition temperatures.

The horizontal dashed line marks the resolution limit of our GISAXS setup that imposes an upper resolution limit to the average nanoclusters distances, while the vertical continuous line marks the border before which the uncertainty forbids to consider the fitted data acceptables. It can be seen that the interference peaks maxima emerge from the X-Ray scattering profiles at $q_{y,max} \approx 1.05\ nm^{-1}$, $q_{y,max} \approx 0.55\ nm^{-1}$ and $q_{y,max} \approx 0.5\ nm^{-1}$ for 50°C, 60°C and 100°C respectively, while for 150°C, 200°C and 300°C there are little deviations respect to the value $q_{y,max} \approx 0.4\ nm^{-1}$. These measurements show that to a decrease of the constant temperature at which was run the deposition corresponds an increase of the value along the q_y vector of the reciprocal space at which the interference peak maximum arise and since 150°C it is possible to assist to a sort of saturation effect with the appearence of the scattering maxima at a more or less constant value of $\approx 0.4\ nm^{-1}$. Considering the GISAXS data relative to the nucleation stages for our set of experiments it is possible to retrieve the value of the density of the nucleation centers through the formula:

$$n = \left(\frac{q_{y,max}}{2\pi}\right)^2 \tag{4.2}$$

Conducting a statistical analysis, for every temperature, on the density of the forming clusters during the nucleation stage it is possible to derive their average nucleation density and the nucleation energy for the material can be calculated thanks to the formula proposed by Kowarik [14] in his work:

$$N_{max} \approx F^{p} exp\left(\frac{E_{nuc}}{K_B T}\right) \tag{4.3}$$

In this formula N_{max} represents the maximum nucleation density of the nanoclusters over the sample surface, while F, K_B and T are the atomic flux impinging on the sample, the Boltzmann constant and the substrate temperature respectively. In fig. 4.2 are shown the nucleation density data in an Arrhenius plot, where the maximum nucleation density of the nanoclusters over the sample surface N_{max} is fitted for the data emerging from the minimum N_{max} background, corresponding to the lattice defect density of the substrate. From the fitting and, more precisely, from the value of the slope of the linear function employed to perform the fit, it is possible to directly extract the nucleation energy E_{nuc} for which we retrieved a value of 303 $meV \pm 172$.

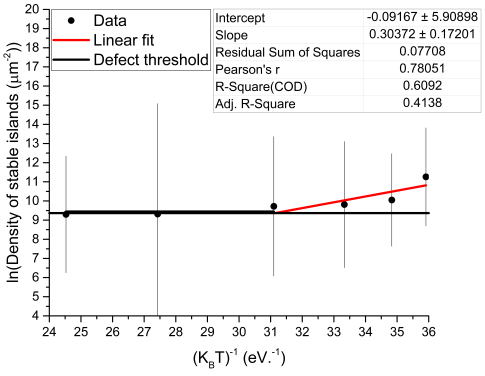

Fig. 4.2: Plot of the natural logarithm of the density of stable islands vs. the inverse of the temperature.

The reduction of the uncertainty over the peak position and its better appearance coincides with the onset of nanoclusters coalescence. In this stage the average distance Δ between the nanoclustes can no more be expressed with the relation $\Delta = \frac{2\pi}{q_{y,max}}$ and a paracrystal model for the nanoclusters spatial distribution must be taken into consideration due to the cumulative character of nanoclusters structural disorder.

$$\Delta = \frac{\pi + \frac{\pi}{1 + \left(\frac{\sigma}{\sigma_0}\right)^{p}}}{q_{y,max}} \tag{4.4}$$

In order to better understand how the temperature is affecting the dynamic

coalescence stage in the real space, the ex-situ AFM images, shown in fig. 4.3, of two samples, produced stopping the depositions at an equivalent thicknesses of the deposited film of 4 nm, have been acquired for the constant deposition temperatures of 50°C and 200°C.

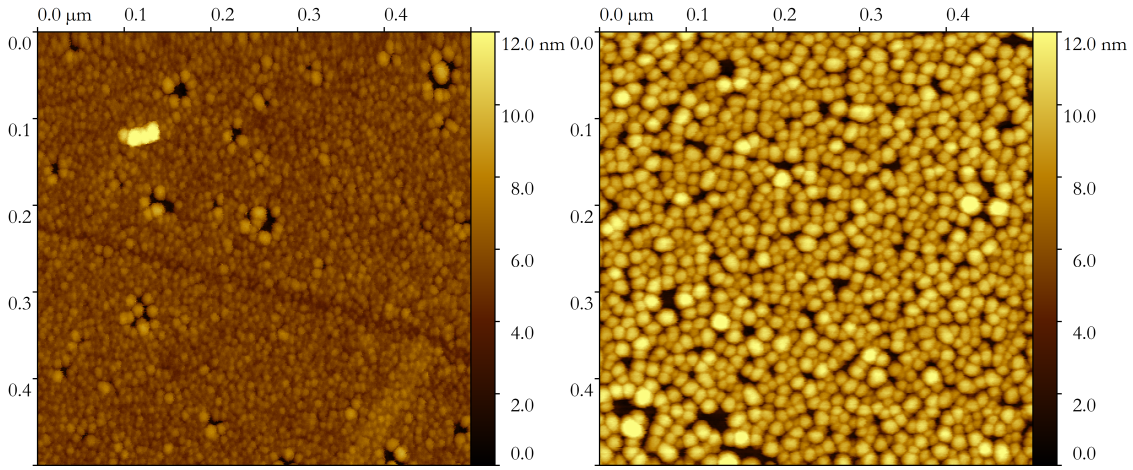

(a) AFM image of copper clusters on graphene deposited at 50°C equivalent to a 4 nm thick continuous layer.

(b) AFM image of copper clusters on graphene deposited at 200°C equivalent to a 4 nm thick continuous layer.

Fig. 4.3: AFM images of samples where a layer with an equivalent thickness of 4nm was deposited. The depositions were stopped during the coalescence stage for two different temperatures.

Estimations gave a nanoclusters surface density of $n \approx 10^{12}\ cm^{-2}$ and $n \approx 3{*}10^{11}\ cm^{-2}$ with an average nanoclusters distance of $\Delta \approx 10\ nm$ and $\Delta \approx 18\ nm$ for 50°C and 200°C respectively. The nanoclusters have a uniform emispherical shape, with the diameter steadily increasing with the temperature. Comparing these results with the ones retrieved from the GISAXS at the same equivalent deposited thickness we find $n \approx 2 * 10^{12}\ cm^{-2}$ and $n \approx 4.5 * 10^{11}\ cm^{-2}$ with an average nanoclusters distance of $\Delta \approx 6\ nm$ and $\Delta \approx 15\ nm$ respectively. The presented results are in good agreement with only slight deviations the ones from the others. Furthermore, they show that to higher temperatures correspond lower surface densities of the nanoclusters and that during the growth they join into bigger islands reducing their surface density at the onset of the coalescence. A careful inspection of the plot in fig. 4.1 suggests two major changes in the rate

of the shift of the interference peak position towards lower values of $q_{y,max}$ for every deposition. This may be connected with the transition from the nucleation stage to the dynamic coalescence one and with the transition from the coalescence to the percolation stage [15]. At the percolation stage, nanoclusters merge into larger clusters of irregular shapes that are displayed in the GISAXS pattern by two well-resolved maxima closer to the primary beam. From the analysis of the rate shift of the $q_{y,max}$ position in function of the deposited thickness and from the ellipsometric measuremens was possible to provide an estimation of thicknesses at which the transitions from the nucleation stage to the dynamic coalescence and from the dynamic coalescence to the percolation occurred. These results are compared in fig. 4.4.

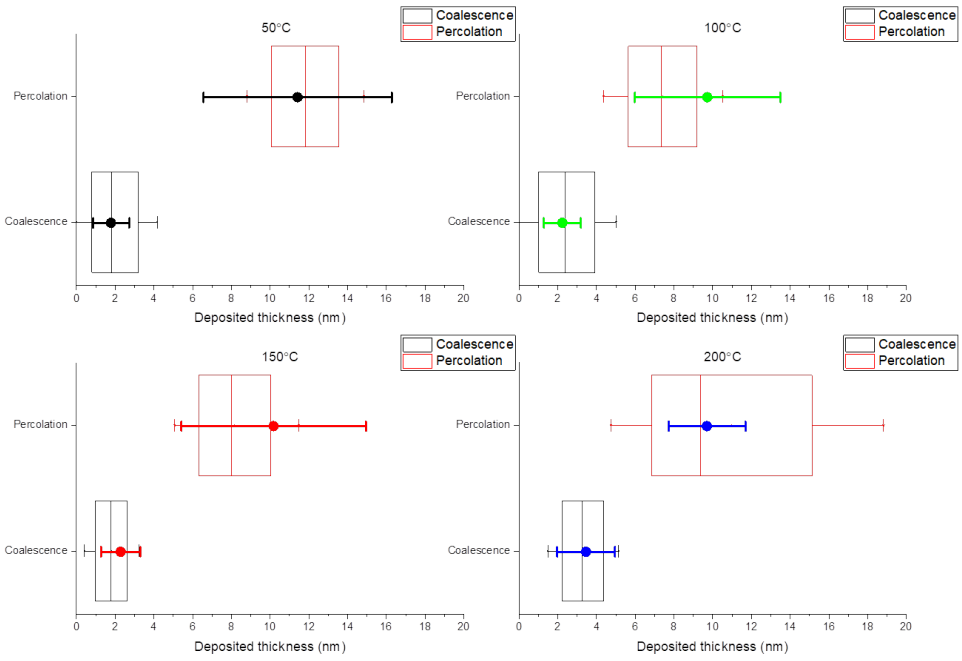

Fig. 4.4: Final comparison of the extracted values for the beginning of the coalescence and of the percolation stages for different temperatures. The box plots indicate the values of the centers of the beginning of a new growing stage with the rescpective uncertainty based on the GISAXS data, while the simple points with their relative error bars indicate the ones based on the ellipsometry data.

The results obtained from the two analysis are in good agreement, especially for what concern the beginning of the coalescence stage that occurs at around 2 nm of Cu equivalent deposited thickness for all the depositing temperatures. More uncertainty surrounds the beginning of the percolation stage that, anyway, can be assumed to occur around 10 nm of Cu equivalent deposited thickness for all the depositing temperatures. Another intersting result is that the beginning of the dynamic coalescence and of the percolation stages are not affected by the temperature as the cluster density or size and occur at the same equivalent thickness of the deposited layer for all the deposition temperatures.

4.2 Thermal evaporation deposition on molybdenum disulphide

This set of experiments was performed with the same goal of the previous one. From the GISAXS intensity maps we can notice that the peaks of interference appear at lower thicknesses for higher temperatures and if at the equivalent layer thickness of 4 nm at 60°C is visible only an intensity streak, for the same thickness the GISAXS pattern shows broad side peaks located at $q_y \approx \pm 0.35\ nm^{-1}$ and $q_y \approx \pm 0.15\ nm^{-1}$ in the case of the depositions performed at 100°C and 150°C respectively. This difference decrease at the increase of the equivalent deposited thickness, at 12 nm it is possible to see a reduction in the distances of the lateral side peaks that are located at $q_y \approx \pm 0.25\ nm^{-1}$, $q_y \approx \pm 0.21\ nm^{-1}$ and $q_y \approx \pm 0.12\ nm^{-1}$ for 60°C, 100°C and 150°C respectively, while at 24 nm the distance between the lateral side maxima in the q_y direction becomes negligible. As previously stated, this phenomenon is due to the fact that the interference effects intensify with the growth of the nanoclusters and their coalescence in bigger islands cause a long range modulation of the electronic density seen from the impinging X-Ray that get scattered towards lower values in the q_y direction. Eventually, after the percolation and the formation of a continuous layer of deposited material, it is no longer possible to distinguish clearly the nucleated islands and for all the samples the morphology of the surfaces look similar and so do the GISAXS patterns. In order to track quantitatively the kinetics of copper growth on MoS_2, we employed the same analysis performed for the depositions on graphene and the position of the gaussian center $q_{y,max}$ is plotted in fig. 4.5 respect to the equivalent Cu deposited thickness. Even for this analysis were expressed with an horizontal

dashed line marks the resolution limit of our GISAXS setup, that imposes an upper resolution limit to the average nanoclusters distances, and with a vertical continuous line the border before which the uncertainty forbids to consider the fitted data acceptables.

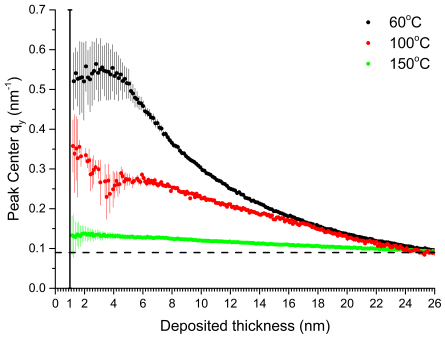

Fig. 4.5: Plot of the $q_{y,max}$ vs. deposited copper thickness for various deposition temperatures.

From fig. 4.5 it is possible to notice that the interference peaks maxima emerge from the X-Ray scattering profiles at $q_{y,max} \approx \pm 0.55\ nm^{-1}$, $q_{y,max} \approx \pm 0.35\ nm^{-1}$ and $q_{y,max} \approx \pm 0.15\ nm^{-1}$ for 60°C, 100°C and 150°C respectively. To an increase of the constant temperature at which is run the deposition corresponds a decrease of the value along q_y at which the interference peak maximum arises. This trend is once again correlated to the mobility over the surface of the adsorbed particles, to the density of defects acting as nucleation centres and to the fact that to a higher temperature corresponds a larger attraction basin of the defects and, therefore, a lower density of nucleating islands, with the ones that favour a more energetic stable configuration acting as major attractor. These islands tend to attract more material because the higher temperature increase the diffusion coefficient along the surface and the mobility of the adsorbed particles, that find bonding to other cluster more energetically favourable, results enhanced. For this reason, the size of the islands is directly proportional to the temperature of the substrate surface and, thank to their volume and their vast number, they introduce a modulation of the electronic density that can be statistically tracked from the scattering pattern detected from the GISAXS. Employing the previously defined equation 4.3 it is possible to calculate the nucleation energy E_{nuc} for the copper particles nucleating over the MoS_2.In fig. 4.6 it is shown the linear relation that fits our nucleation data in an Arrhenius plot, where the ln(N) is represented versus the inverse of the temperature [14]. From the fitting and more precisely from the value of slope of the linear function employed to perform the fit, was calculated a nucleation energy value of 377.7 $meV \pm 6.6$.

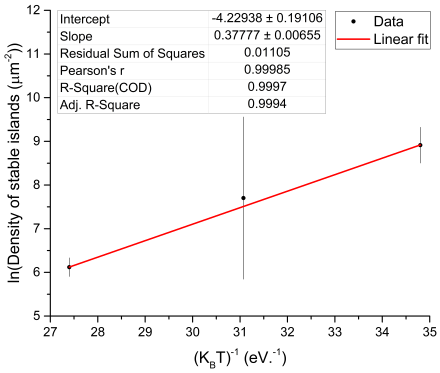

Fig. 4.6: Plot of the natural logarithm of the density of stable islands vs. the inverse of the temperature.

As already found in the case of the depositions on graphene, even the fast nucleation process of copper nanoclusters on MoS_2 following from our GISAXS analysis suggests a high surface density of nucleation centres, typical for heterogeneous nucleation at surface defects and impurities. The coalescence stage was studied even in the real space frame stopping the depositions at a constant thicknesses of 4 nm and acquiring an AFM image for every previously considered temperature. These images are displayed in fig. 4.7 and, from their further elaboration and analysis, was possible to estimate the pair correlation functions of the nanoclusters showed in fig. 4.8 corresponding to the inquired temperatures.

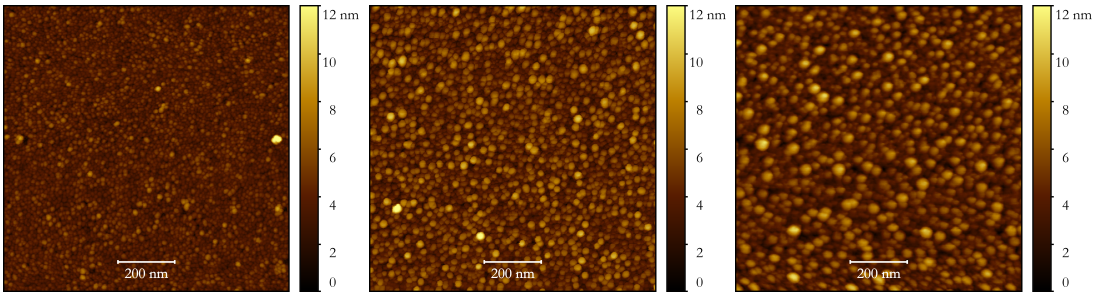

(a) AFM image of copper clusters on MoS_2 deposited at 60°C equivalent to a 4 nm thick continuous layer.

(b) AFM image of copper clusters on MoS_2 deposited at 100°C equivalent to a 4 nm thick continuous layer.

(c) AFM image of copper clusters on MoS_2 deposited at 150°C equivalent to a 4 nm thick continuous layer.

Fig. 4.7: AFM images of samples where a layer with an equivalent thickness of 4nm was deposited. The depositions were stopped during the coalescence stage for all the different temperatures.

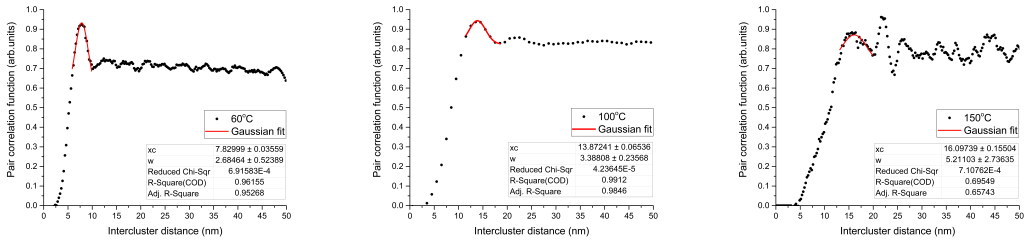

(a) Pair correlation function of the copper clusters retrieved from the AFM image of the deposition performed on MoS_2 at 60°C.

(b) Pair correlation function of the copper clusters retrieved from the AFM image of the deposition performed on MoS_2 at 100°C.

(c) Pair correlation function of the copper clusters retrieved from the AFM image of the deposition performed on MoS_2 at 150°C.

Fig. 4.8: Pair correlation function with the fitting of their first maxima retrieved from the AFM images of the samples where a layer with an equivalent thickness of 4nm was deposited.

The first maximum of each one of these functions represent the average distance between first neighbours and their fittings return the values of $\Delta \approx 8\ nm$, $\Delta \approx 14\ nm$ and $\Delta \approx 16\ nm$ that correspond to a nanoclusters surface density of $n \approx 1.5{*}10^{12}\ cm^{-2}$, $n \approx 5{*}10^{11}\ cm^{-2}$ and $n \approx 4{*}10^{11}\ cm^{-2}$ for 60°C, 100°C and 150°C respectively. This is perfectly coherent with the fact that a wider range of values for the dimension of the particle corresponds to a faster dynamics. Anyway, if we now compare these results with the ones retrieved from the GISAXS measurements corresponding to the same equivalent deposited thickness, it is possible to notice a huge divergence even in the ratio between the results in the set obtained with the same measurement. After an analysis similar to the one performed on the grapene samples, the temperature seems to affect the thickness at which the nucleation is occurring, around 2 nm, 4 nm and 5 nm for 150°C, 100°C and 60°C respectively. While, from these data it is hard to identify a threshold for the onset of the percolation stage but a further changing in the slope of the nanoclusters average distances versus the deposited thickness of copper around 17 nm for the depositions at 60°C and 100°C suggests that at this thickness the percolation must have already taken place for all the temperatures.

5. LIST OF PUBLICATIONS

5.1 Publications in CC journals

- PELLETTA, Marco - ŠIFFALOVIČ, Peter - HALAHOVETS, Yuriy - BRNDIAROVÁ, Jana - SHAJI, Ashin - JERGEL, Matej - MAJKOVÁ, Eva. In-situ analysis of copper growth kinetics on MoS_2. Pending review.

- HODAS, Martin - ŠIFFALOVIČ, Peter - JERGEL, Matej - PELLETTA, Marco - HALAHOVETS, Yuriy - VÉGSÖ, Karol - KOTLAR, Mário - MAJKOVÁ, Eva. Kinetics of copper growth on graphene revealed by time-resolved small-angle X-Ray scattering. In Phys. Rev. B, 2017, Vol. 95, Iss. 3, pag. 035424.

- SZOBOLOVSZKY, Robert - ŠIFFALOVIČ, Peter - HODAS, Martin - PELLETTA, Marco - JERGEL, Matej - SABOL, Dušan - MÁCHA, Marek - MAJKOVÁ, Eva. Waste heat recovery in solid-state lighting based on thin film thermoelectric generators. In Sustainable Energy Technologies and Assessments, 2016, Vol. 18, Pag. 1-5

- VÉGSÖ, Karol - JERGEL, Matej - ŠIFFALOVIČ, Peter - KOTLAR, Mário - HALAHOVETS, Yuriy - HODAS, Martin - PELLETTA, Marco - MAJKOVÁ, Eva. Real-time SAXS study of a strain gauge based on a self-assembled gold nanoparticle monolayer. In Sensors and Actuators A: Physical, 2016, Vol. 241, Pag. 87-95

- KOSTIUK, Dmytro - BODÍK, Michal - ŠIFFALOVIČ, Peter - JERGEL, Matej - HALAHOVETS, Yuriy - HODAS, Martin - PELLETTA, Marco - PELACH, Michal - HULMAN, Martin - ŠPITÁLSKY, Zdenko - OMASTOVÁ, Mária - MAJKOVÁ, Eva. Reliable determination of the few-layer graphene

oxide thickness using Raman spectroscopy. In Journal of Raman Spectroscopy, 2016, Vol. 47, Iss. 4, Pag. 391-394

- HODAS, Martin - ŠIFFALOVIČ, Peter - HALAHOVETS, Yuriy - PELLETTA, Marco - VÉGSÖ, Karol - JERGEL, Matej - MAJKOVÁ, Eva. In-situ GISAXS monitoring of ultrashort period W/B_4C multilayer X-ray mirror growth. In Proceedings SPIE, 2015, Vol. 9588, Advances in X-Ray/EUV Optics and Components X, Pag. 958804

- ŠIFFALOVIČ, Peter - BADÁŇOVÁ, Dominika - VOJTKO, Andrej - JERGEL, Matej - HODAS, Martin - PELLETTA, Marco - SABOL, Dušan - MÁCHA, Marek - MAJKOVÁ, Eva. Evaluation of low-cadmium ZnCdSeS alloyed quantum dots for remote phosphor solid-state lighting technology. In Applied Optics , 2015, Vol. 54, Iss. 23, Pag. 7094-7098

- HODAS, Martin - ŠIFFALOVIČ, Peter - PELLETTA, Marco - HALAHOVETS, Yuriy - JERGEL, Matej - MAJKOVÁ, Eva - KORYTÁR, Dušan - ZÁPRAŽNÝ, Zdenko - VAGOVIČ, Patrik. Passivation of Ge crystals by B_4C thin layer deposition. In Proceedings 21th International Conference on Applied Physics of Condensed Matter, 2015.

5.2 Publications in book's chapters

- ŠIFFALOVIČ, Peter - VÉGSÖ, Karol - HODAS, Martin - JERGEL, Matej - HALAHOVETS, Yuriy - PELLETTA, Marco - KORYTÁR, Dušan - ZÁPRAŽNÝ, Zdenko - MAJKOVÁ, Eva. In-Situ X-ray Reciprocal Space Mapping for characterization of Nanomaterials. In In Situ X-Ray Reciprocal Space Mapping for Characterization of Nanomaterials, 2016, pp 507-544

5.3 Conference's contributions

- PELLETTA, Marco - ŠIFFALOVIČ, Peter - HODAS, Martin - HALAHOVETS, Yuriy - VÉGSÖ, Karol - JERGEL, Matej - MAJKOVÁ, Eva. Lecture: In-Situ Real-Time X-Ray Study of Copper Growth on Graphene. E-MRS Spring Meeting and Exhibit 2017, Palais de la Musique et des Congrès, Strasbourg, France.

- PELLETTA, Marco - ŠIFFALOVIČ, Peter - HODAS, Martin - HALAHOVETS, Yuriy - VÉGSÖ, Karol - JERGEL, Matej - MAT'KO, Igor - ZÁPRAŽNÝ, Zdenko - KORYTÁR, Dušan - KECKES, Jozef - DICK, Thomas - MAJKOVÁ, Eva. Lecture: Protective and reflective coatings for soft and hard X-Rays applied to single-point diamond processed surfaces. E-MRS Fall Meeting 2015 & Materials Weekend, Warsaw University of Technology, Warsaw, Poland.

- PELLETTA, Marco - HODAS, Martin - ŠIFFALOVIČ, Peter - HALAHOVETS, Yuriy - VÉGSÖ, Karol - KORYTÁR, Dušan - JERGEL, Matej - MAJKOVÁ, Eva. Lecture: Protective B_4C Layers for High Performance Diffractive X-ray Optics 9th European NESY Winterschool & Symposium on Neutron and Synchrotron Radiation, JUFA Altaussee in Styria, Altaussee, Austria.

- PELLETTA, Marco - HODAS, Martin - ŠIFFALOVIČ, Peter - JERGEL, Matej - HALAHOVETS, Yuriy - MAJKOVÁ, Eva. Poster: Ion beam deposition of advanced multilayer X-Ray mirrors. Workshop on X-ray Scattering Methods for Thin Film Characterization, Charles University, Prague, Czech Republic.

References

1. Kostya S Novoselov, Andre K Geim, Sergei V Morozov, D Jiang, Y Zhang, Sergey V Dubonos, Irina V Grigorieva, and Alexandr A Firsov. Electric field effect in atomically thin carbon films. *Science*, 306(5696):666–669, 2004.

2. Wencai Ren and Hui-Ming Cheng. The global growth of graphene. *Nature nanotechnology*, 9(10):726–730, 2014.

3. Kayci M. Radenovic A. Kis A. Lopez-Sanchez O., Lembke D. Ultrasensitive photodetectors based on monolayer MoS_2. *Nature Nanotechnology*, 8:497–501, 2013.

4. Daria Krasnozhon, Dominik Lembke, Clemens Nyffeler, Yusuf Leblebici, and Andras Kis. MoS_2 transistors operating at gigahertz frequencies. *Nano letters*, 14:5905–5911, 2014.

5. Wissam A. Saidi. Density functional theory study of nucleation and growth of pt nanoparticles on $MoS_2(001)$ surface. *Crystal Growth & Design*, 15(2):642–652, 2015.

6. Wissam A. Saidi. Trends in the adsorption and growth morphology of metals on the $MoS_2(001)$ surface. *Crystal Growth & Design*, 15(7):3190–3200, 2015.

7. Rolf Landauer. Spatial variation of currents and fields due to localized scatterers in metallic conduction. *IBM Journal of Research and Development*, 1(3):223–231, 1957.

8. Yu. V. Sharvin. A possible method for studying Fermi surfaces. *Journal of Experimental and Theoretical Physics*, 21(3):655–656, 1965.

9. Christensen T. M. Physics of thin films: Film formation II. https://www.uccs.edu/ tchriste/courses/PHYS549/549lectures/film2.html, 2001.

10. Dogarari research institute. Growth of nuclei and formation of continuous thin film. http://marriott.tistory.com/128, 2012.

11. S J Gurman. Electron density of states of thin copper films. *Journal of Physics F: Metal Physics*, 5(11):L194, 1975.

12. Daniel Bonn, Jens Eggers, Joseph Indekeu, Jacques Meunier, and Etienne Rolley. Wetting and spreading. *Rev. Mod. Phys.*, 81:739–805, 2009.

13. S. K. Mahatha and Krishnakumar S. R. Menon. Growth and photoemission spectroscopic studies of ultrathin noble metal films on graphite. *Pramana*, 84(6):1011–1022, 2015.

14. Stefan Kowarik. Thin film growth studies using time-resolved x-ray scattering. *Journal of Physics: Condensed Matter*, 29(4):043003, 2017.

15. M. Hodas, P. Siffalovic, M. Jergel, M. Pelletta, Y. Halahovets, K. Vegso, M. Kotlar, and E. Majkova. Kinetics of copper growth on graphene revealed by time-resolved small-angle x-ray scattering. *Phys. Rev. B*, 95:035424, 2017.